Dalton Transactions

ROYAL SOCIETY OF CHEMISTRY

PAPER

View Article Online
View Journal | View Issue

Cite this: *Dalton Trans.*, 2020, **49**, 7903

Polypyrrole coated δ-MnO_2 nanosheet arrays as a highly stable lithium-ion-storage anode†

Yiming Sui,[a,b] Chaofeng Liu,[a] Peichao Zou,[b] Houchao Zhan,[b] Yuanzheng Cui,[b] Cheng Yang*[b] and Guozhong Cao *[a]

Received 7th May 2020,
Accepted 14th May 2020

DOI: 10.1039/d0dt01658f

rsc.li/dalton

Manganese dioxide (MnO_2) with a conversion mechanism is regarded as a promising anode material for lithium-ion batteries (LIBs) owing to its high theoretical capacity (~1223 mA h g^{-1}) and environmental benignity as well as low cost. However, it suffers from insufficient rate capability and poor cyclic stability. To circumvent this obstacle, semiconducting polypyrrole coated-δ-MnO_2 nanosheet arrays on nickel foam (denoted as MnO_2@PPy/NF) are prepared *via* hydrothermal growth of MnO_2 followed by the electrodeposition of PPy on the anode in LIBs. The electrode with ~50 nm thick PPy coating exhibits an outstanding overall electrochemical performance. Specifically, a high rate capability is obtained with ~430 mA h g^{-1} of discharge capacity at a high current density of 2.67 A g^{-1} and more than 95% capacity is retained after over 120 cycles at a current rate of 0.86 A g^{-1}. These high electrochemical performances are attributed to the special structure which shortens the ion diffusion pathway, accelerates charge transfer, and alleviates volume change in the charging/discharging process, suggesting a promising route for designing a conversion-type anode material for LIBs.

1 Introduction

Lithium-ion batteries (LIBs) are the most important energy storage devices and have shown rapid advancement in the past few decades to meet larger demands on electric power and advanced portable electronics.[1,2] Anodes, as one critical component in LIBs, may play a determining role in the overall performances, including cyclic stability, reversible capacity, energy/power density, *etc*.[3] While the current graphite anode working with an intercalation mechanism enjoys widespread commercial success, it suffers from limited capacity (theoretically ~372 mA h g^{-1}). It is therefore imperative to explore alternative anode materials.[4,5]

Transition metal oxides (Fe_2O_3, V_2O_3, MnO_2, *etc.*) working with a conversion mechanism can in principle deliver much higher theoretical capacity than their graphite anode counterparts, even exceeding 1000 mA h g^{-1}, and also exhibit suitable working potential to achieve the goal of high energy density.[3,6–10] Among the high-capacity anode materials, MnO_2 receives extensive attention due to its great earth abundance, low price and high theoretical capacity (1223 mA h g^{-1}).[6,11] However, this conversion reaction involves a dramatic structural/volume change, low coulombic efficiency, and large voltage hysteresis, all of which jeopardize the overall electrochemical performance of the cells.[6] To mitigate such problems and improve their electrochemical performances, various techniques have been investigated. One strategy is by encapsulating or sandwiching manganese dioxides within conducting materials like graphene[12] and hollow carbon spheres[13] as anode composites, in which the conductive coating improves the overall electrical conductivity and provides physical confinement for volume change. However, the electrodes based on these materials are typically prepared through coating slurry on current collectors, in which the insulating binder hampers the rate capability by blocking the Li^+ diffusion routes and hindering the electrical conductivity.[14] Another approach is by growing nano- or micro-sized particles over a 3D conductive substrate, which could effectively shorten the diffusion route of Li^+ and increase the contact area with conducting substances in electrodes or electrolytes, which are favorable for releasing the stress generated by Li^+ insertion and promoting the rate performance and cycling stability.[15–17] However, the short cycling life of the binder-free electrodes obtained by the pulverization of active materials is also fatal and overshadows their advantages.[18] However, combining both strategies to prepare conductive-material coated binder-free MnO_2 nanomaterial electrodes could be an effective approach to circumvent the obstacles to achieve high battery performance.

[a]*Department of Materials Science and Engineering, University of Washington, Seattle, WA 98195, USA. E-mail: gzcao@uw.edu*
[b]*Division of Energy and Environment, Tsinghua Shenzhen International Graduate School, Tsinghua University, Shenzhen 518055, China. E-mail: yang.cheng@shenzhen.tsinghua.edu.cn*

†Electronic supplementary information (ESI) available. See DOI: 10.1039/D0DT01658F

Limited works have been reported so far on this route, partially due to the synthesis complexity of the strategy.[19–21]

In the present study, δ-MnO_2 nanosheets were *in situ* grown on the surface of NF and subsequently coated with a uniform PPy layer *via* electrodeposition. In comparison with other methods (*e.g.* oxidative polymerization[22] and vapor phase polymerization[23]), electrodeposition could not only induce polymerization under mild conditions without excess products or toxics but also precisely control the polymerization speed and the thickness of PPy.[24] The growth mechanism of δ-MnO_2 nanosheets, PPy deposition parameter optimization and their potential for application as an anode material in LIBs have been discussed. Such a structure facilitates Li^+ diffusion and withstands volume variation. It also provides a large specific surface area for rapid redox reactions. PPy coating could help maintain the nanosheet integrity by offering mechanical support and enhance electronic conductivity.[25] Owing to the synergistic effect of the nano-structured morphology of MnO_2 particles, conductive PPy coating and porous NF substrates, the MnO_2@PPy/NF electrode with a coating thickness of ~50 nm could deliver a reversible capacity of ~1240 mA h g^{-1} at 0.1 A g^{-1}, good cycling stability with over 95% capacity retention after 120 cycles at a current rate of 0.43 A g^{-1} and a capacity of ~430 mA h g^{-1} at a current density of 2.67 A g^{-1}.

2 Experimental

2.1 Synthesis of δ-MnO_2 nanosheets on NF

The nickel foam (NF) was cut into a circular disk with a radius of 5 mm, followed by supersonic cleaning for 15 minutes separately in acetone, deionized water, hydrochloric acid (3 M), and deionized water to remove the organic residues and oxide layer on the surface. Then, the cleaned NF was dried in a vacuum oven at 60 °C overnight. Thereafter, 1 mmol of $KMnO_4$ was dissolved in 20 mL of deionized water under vigorous stirring, and the as-obtained solution was transferred to a 30 mL Teflon autoclave with 3 pieces of cleaned NF immersed inside. Afterwards, the autoclave was sealed and placed in a muffle oven to maintain at 180 °C for 3 hours. Finally, the resulting samples were washed with deionized water and ethanol, respectively, and dried at 60 °C for 24 hours. The obtained composite material was denoted as MnO_2/NF.

2.2 Electrodepositing PPy coating

0.1 mL of the pyrrole monomer was added into 10 mL of Na_2CO_3 solution (0.1 M) drop by drop under vigorous stirring. The mixture was used as an electrolyte combined with a MnO_2/NF working electrode, platinum counter electrode and Ag/AgCl reference electrode. The operating potential was set at 1.2 V (*vs.* Ag/AgCl) and the electrodeposition lasted for 50 s and 150 s; the corresponding products were denoted as MnO_2@PPy/NF-50 and MnO_2@PPy/NF-150, respectively. Subsequently, the samples were cleaned with deionized water and ethanol and dried at 60 °C in a vacuum oven for 12 hours.

2.3 Material characterization

X-ray diffraction (XRD) was performed by using a Bruker X-ray diffractometer (D8 Discover with a IμS 2-D detection system) at an accelerating voltage of 50 kV and a working current of 1000 μA, using a Cu–K_α radiation source at an angle from 10.5 to 98.5° and the initial wavelength was set at 6800 nm in order to avoid the fluorescence effect of element manganese within the samples. The morphology and the size of the particles were obtained *via* scanning electron microscopy (SEM, Sirion XL30), atomic force microscopy (AFM) and transmission electron microscopy (TEM, FEI Spirit T12). A Kratos Axis Ultra DLD X-ray photoelectron spectroscopy system (XPS) was used to confirm the surface element/bonding/valence state compositions. The Brunauer–Emmett–Teller (BET) theory *via* nitrogen adsorption/desorption was also employed to measure the surface area of the samples. The functional group and bonding information were collected using a Fourier transform infrared spectrometer (FT-IR, Bruker, VERTEX 70).

2.4 Electrochemical measurements

The galvanostatic tests were conducted by using a NEWARE tester (CT-4008) between 0.01 and 3 V (*vs.* Li/Li^+), and the EIS measurements were performed in a frequency range between 10^5 and 0.01 Hz. During cell assembly, the material we studied was used as the working electrode, paired with lithium metal foil as the counter electrode, 2 pieces of polypropylene film (Celgard 2400) as the separator and a mixed solution containing 1 M $LiPF_6$ dissolved in ethyl carbonate (EC)/dimethyl carbonate (DMC) (1 : 1 V : V) as the electrolyte. The redox characteristics of the material were studied by cyclic voltammetry (CV) using a Solartron electrochemical station (SI 1287) with a voltage window between 0.01 V and 3 V at different scan rates.

3 Results and discussion

3.1 Material synthesis mechanism

Fig. 1 illustrates the synthesis process of the MnO_2@PPy/NF electrode. In the first step, the NF is ultrasonically washed with acetone, deionized water, hydrochloric acid, and deionized ethanol in sequence to remove the organic residue and oxide layer on the surface. The cleaned NF is then immersed in a $KMnO_4$ solution which undergoes a hydrothermal process to grow δ-MnO_2 nanosheets on its surface. During the process, in basic solutions (pH = 7.4 for the 0.05 M $KMnO_4$ aqueous electrolyte) and at 180 °C, both the NF substrate and the water in solutions will be oxidized into NiO and O_2, respectively, and $KMnO_4$ will be reduced into MnO_2. Afterwards, the as-synthesized MnO_2/NF undergoes electrodeposition to obtain the MnO_2@PPy/NF electrode, in which the pyrrole monomers in the electrolytes are induced to polymerize by external electric current which leads to an even PPy coating on the material surface.

Two redox steps occur during the hydrothermal process as shown in eqn (1) and (2), respectively. Firstly, both reactions are favored by thermodynamic calculations. Specifically, both

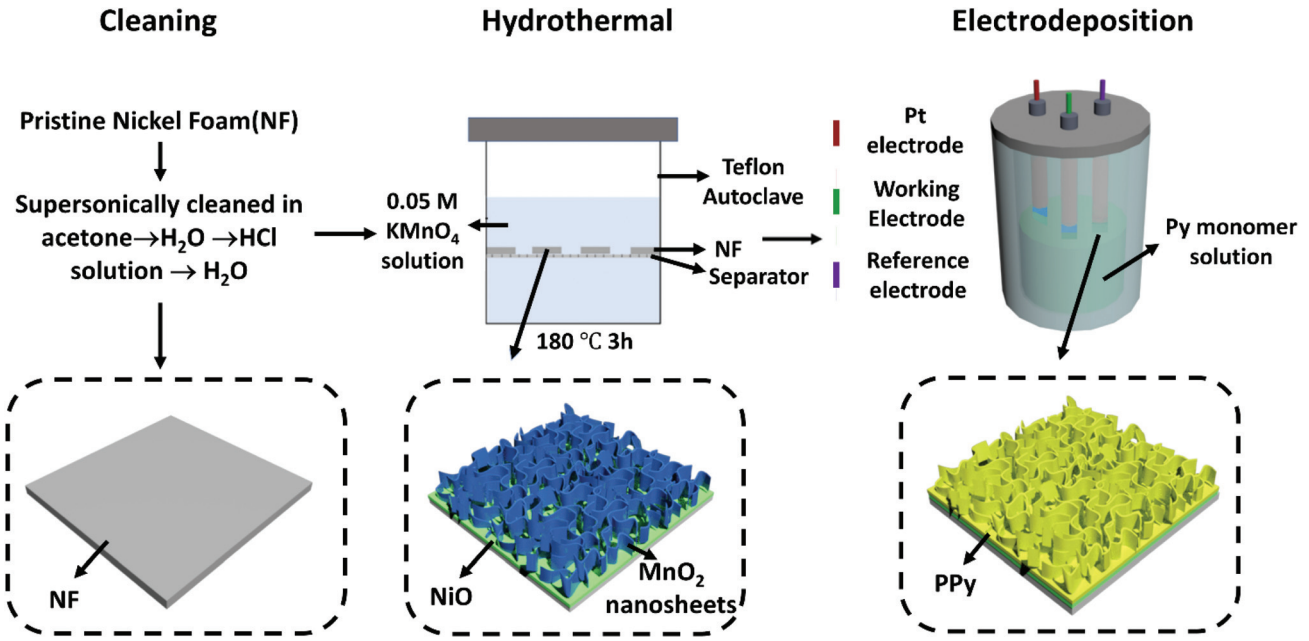

Fig. 1 Schematic illustration of the synthesis process of MnO_2@PPy nanosheet arrays on NF including the NF cleaning process (left), MnO_2 nanosheet growth over NF through a hydrothermal process (middle) and PPy electrodeposition (right).

redox reaction equations could be divided into two independent half reactions (*i.e.* eqn (1) → eqn (3) and (4); eqn (2) → eqn (3) and (5)) and the standard reaction potential for the two redox reactions (denoted as E_0) could be derived by adding the standard reaction potential of the corresponding half reactions together.[26] Furthermore, the real potentials for the two overall reactions under the working conditions (denoted as E) are calculated *via* the classic Nernst equation (see eqn (6)) and transferred to Gibbs free energy through eqn (7), in which R is the universal gas constant, T is the working temperature, Z is the transference number of electrons in the reaction, F is the Faraday constant and Q stands for the concentration ratio of the components in the redox reaction. It turns out that the calculated Gibbs free energy values for both reactions are below zero, proving their spontaneous occurrence under hydrothermal conditions.[27–30]

$$H_2O + 2MnO_4^- + 3Ni \rightarrow 3NiO + 2MnO_2 + 2OH^- \quad (1)$$

$$2H_2O + 4MnO_4^- \rightarrow 4MnO_2 + 4OH^- + O_2\uparrow \quad (2)$$

$$MnO_4^- + 2H_2O + 3e^- \rightarrow MnO_2 + 4OH^- \quad E_h = 0.59\ V \quad (3)$$

$$2OH^- + Ni - 2e^- \rightarrow NiO + H_2O \quad E_h = 0.0874\ V \quad (4)$$

$$O_2 + 4e^- + 2H_2O \rightarrow 4OH^- \quad E_h = 0.401\ V \quad (5)$$

$$E = E_0 - \frac{RT}{ZF}\ln(Q_R) \quad (6)$$

$$\Delta G = -nEF \quad (7)$$

In addition, the composition of the composite material (δ-MnO_2/NF) after the hydrothermal reaction is also characterized by XRD, XPS, EDS and CV, and the corresponding patterns are shown in Fig. 2. In the XRD pattern (Fig. 2a), the two sharp peaks at 44.4° and 52.1° correspond to the (111) and (200) planes of the nickel metal substrate, respectively. The other four main peaks at 12.3°, 24.8°, 36.6° and 65.5° can be assigned to the (003), (006), (101), (110) planes of birnessite-type MnO_2, respectively (PDF 00-052-0556).[26,31] δ-MnO_2 possesses a layered structure, which is composed of octahedral MnO_6 and accommodates potassium ions between the adjacent layers (Fig. 2b). The absence of featured peaks for the NiO phase is partially due to its low mass ratio in the composite material or low crystallinity.[26,31] The XPS results reveal detailed information on the composition of the composites. Firstly, the broad survey scan demonstrates the coexistence of Mn, O, K, and Ni elements in MnO_2/NF (see Fig. 2c). Moreover, Mn accounts for ~20 at% in the composite while the element Ni accounts only for ~7 at%, which partially explains the absence of featured peaks for NiO in the XRD pattern. In the high-resolution Mn 2p spectrum, the peaks at 641.91 eV, 642.6 eV, and 643.8 eV are assigned to the existence of Mn^{3+}, Mn^{4+}, and Mn^{5+}, respectively (Fig. 2d). To note, the existence of Mn^{3+} in the MnO_2 crystals helps to achieve the overall electric neutrality by compensating for the extra positive charges produced by Mn^{5+}, intercalated K^+ and oxygen vacancies.[32] The rich Mn and O vacancies in the MnO_2 crystal could tune its electronic structure and improve the electronic conductivity.[33] At the same time, the EDS pattern confirms the elements in the composite to be Mn, K, O, and Ni, which coincides with the results from XPS analysis (Fig. 2e). In addition, some more information about the material composition of δ-MnO_2/NF can also be obtained by the presence of distinct peaks in the CV curve

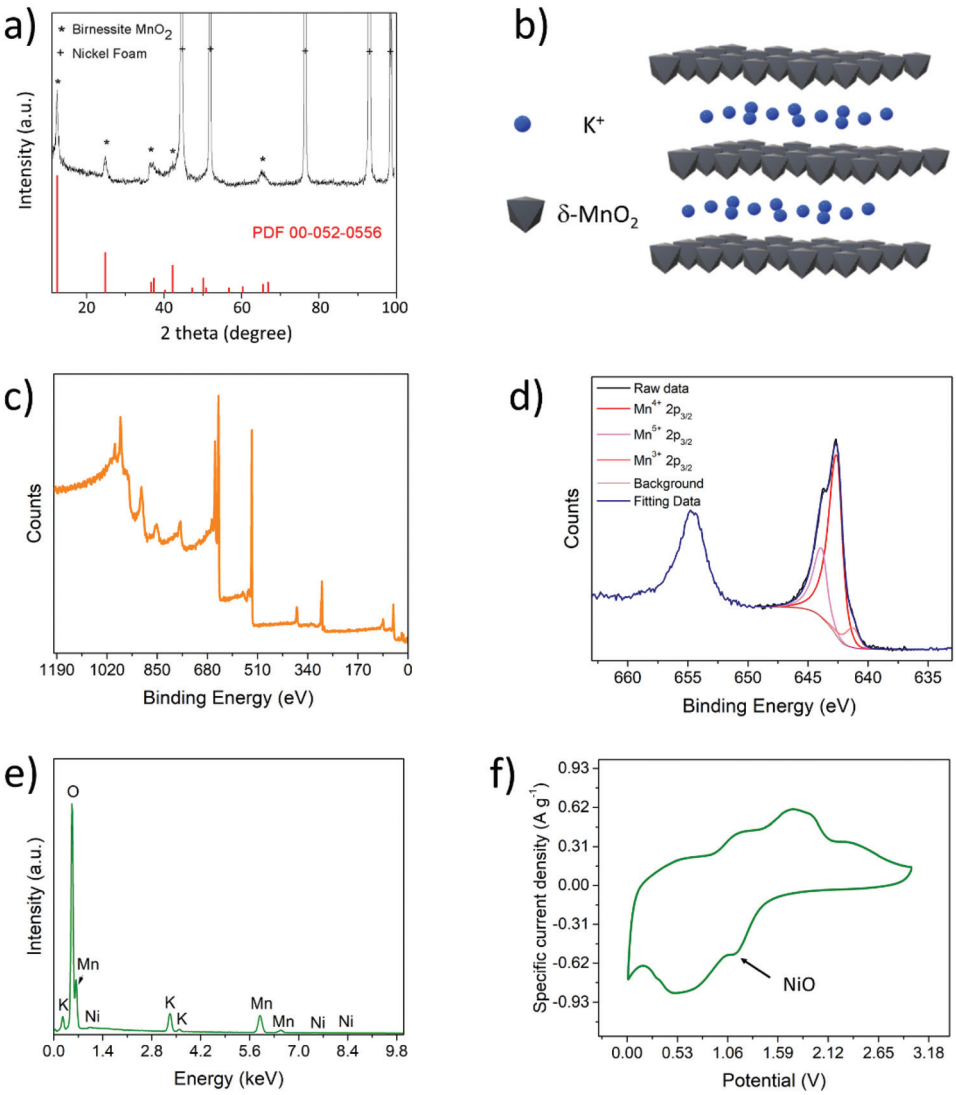

Fig. 2 Structural characterization of MnO_2/NF: (a) XRD pattern of the composite material. (b) Schematic illustration of the δ-MnO_2 structure. (c) XPS survey scan. (d) High resolution XPS scan of the Mn $2p_{3/2}$ peaks. (e) EDS pattern of the composite material. (f) CV curve for the material cycling at a rate of 0.2 mV s^{-1} between 0.01 V and 3 V (*vs.* Li/Li^+).

(Fig. 2f). To be specific, the peaks at 1.12 V in the cathodic scan and 1.9 V in the anodic scan matched the conversion reactions of NiO, which offers solid evidence to prove the coexistence of MnO_2 and NiO.[34] To note, other electrochemical features related to the CV curves will be discussed in detail in the following sections.

In addition to the thermodynamic calculations and direct characterization of the material composition, pH of the solution is measured before and after the prolonged hydrothermal reaction from 3 h to 9 h and a significant increase of pH from 7.4 to 12 is noticed, which accords with the constant production of OH^- in both reactions. Besides, the products of the 0.05 M $KMnO_4$ solution after the hydrothermal reaction under the same experimental conditions are collected, washed, and freeze-dried. The XRD (Fig. S1†) and EDS (Fig. S2†) results prove that the material derived from the $KMnO_4$ decomposition is also δ-MnO_2. Considering the mass ratio of NiO in the composite material, MnO_2 is majorly contributed from eqn (2). Therefore, in combination with the related literature, a general formation mechanism can be proposed.[26,35–37] In the initial state, the surface of NF is oxidized by $KMnO_4$ to form a composite layer of δ-MnO_2 and NiO, and this layer blocks the further reaction between the bare nickel metal and $KMnO_4$. Afterwards, the decomposition of $KMnO_4$ becomes the dominant reaction and constantly contributes MnO_2 to the previously formed MnO_2 nuclei. Finally, δ-MnO_2 grows into a thermodynamically favored nanosheet structure with a slightly warped edge.[32,35,38]

The pyrrole monomers are electrochemically induced to polymerize on the surface of the MnO_2/NF electrode which gradually leads to the formation of an even and uniform layer of PPy coating (affording MnO_2@PPy/NF electrode), following

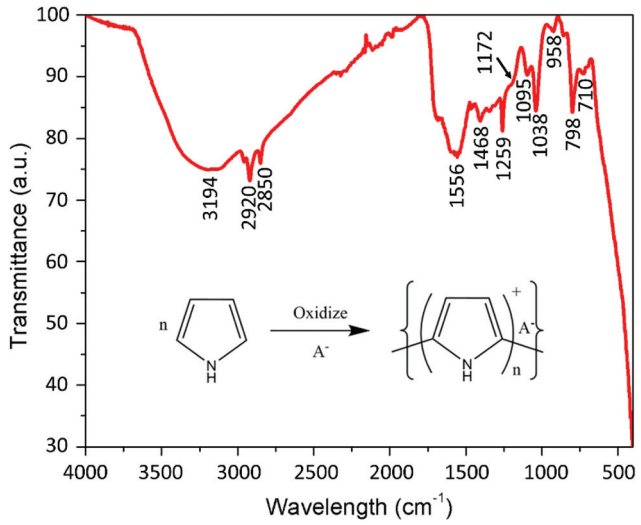

Fig. 3 FTIR spectrum of the MnO_2@PPy/NF sample (the inset shows the reaction equation of the pyrrole monomer polymerizing into PPy).

the reaction equation in Fig. 3.[22] The electrodeposition potential is set at 1.2 V (*vs.* Ag/AgCl) since the PPy produced by this method exhibits the optimum electric conductivity in the potential range between 0.8 and 1.2 V (*vs.* Ag/AgCl).[24] Fig. S3† displays the chronoamperometric graph for the electrodeposition process (the purple curve), which is distinct from the typical one of the planar electrode and clearly consists of two stages with a critical time of 50 s.[39,40] In the first stage, the Py monomers mainly polymerize on the NiO/NF substrates due to the better electric conductivity than their MnO_2 nanosheet counterparts (the green curve). The decreased current with time follows the I–$t^{1/2}$ trend, which is ascribed to the limited diffusion capability of the Py monomers in the electrolytes.[40,41] In the second stage, the Py monomer polymerization over their MnO_2 nanosheet counterparts begins to dominate due to the more facile supplement of the Py monomers (the orange curve). After 150 s deposition, the overall current drops to a value close to zero and remains constant afterwards, during which the rates of PPy growth and thickening are already very low. That is why we study the impact of PPy coating on the electrochemical performances of the composite electrodes with two types of samples (MnO_2@PPy/NF-50 and MnO_2@PPy/NF-150). To characterize the deposited composition, FTIR spectroscopy is carried out for the powder scratched from nickel foil after the hydrothermal reaction and electrodeposition. In Fig. 3, the peaks at 1172 cm^{-1} and 720 cm^{-1} are due to MnO_2 in the composites[42] and the peaks at 3194 cm^{-1}, 2950 cm^{-1}, 2920 cm^{-1} and 2850 cm^{-1} correspond to hydroxyl vibration modes, 1556 cm^{-1} to antisymmetric pyrrole ring vibration, 1480 cm^{-1} to symmetric pyrrole ring vibration, the peaks at 1403 cm^{-1}, 1330 cm^{-1}, and 1259 cm^{-1} to the C–N stretching vibration, 1095 cm^{-1} to =C–H, 1038 cm^{-1} to N–H in-plane deformation vibration, 958 cm^{-1} to the out-of-plane vibration of C–H, 878 cm^{-1} and 798 cm^{-1} to the out-of-plane deformation vibration of C–H,[24,25,43–46] confirming the formation of PPy coating.

3.2 Microstructure

The materials with different PPy depositing times are characterized by FE-SEM and AFM. The NF substrate shows a smooth surface, in comparison with the rough surface morphology after *in situ* growing the MnO_2 nanosheets and depositing the PPy coating (see Fig. S4–S6† and Fig. 4a–f). Besides, the high magnification SEM and AFM images of the bare MnO_2/NF sample (Fig. 4b and c) also display a clear warped edge for the nanosheets, which has already been discussed above. After the PPy electrodeposition and extension of the deposition time, the material surface gets rougher (Fig. S5, S6† and Fig. 4e and f), which partially reflects the successful deposition of PPy coating. Furthermore, TEM is carried out for both the bare MnO_2 nanosheets and MnO_2@PPy nanosheets at a deposition time of 150 s, which are prepared by separately scratching them off the nickel substrate directly after the hydrothermal reaction and electrodeposition. As shown in Fig. 4g, a hierarchical structure could be directly observed with the thickness of PPy coating of approximately 40–50 nm at an electrodeposition time of 150 s. Under the high resolution TEM (HRTEM), the distance between adjacent lattices is ~0.24 nm which is in agreement with the spacing of the (111) plane of δ-MnO_2 (Fig. 4h), again demonstrating the composition of the nanosheets to be δ-MnO_2.[26]

3.3 Electrochemical performances

The electrochemical lithium storage performance of the as-synthesized material (MnO_2@PPy/NF) was first evaluated through galvanostatic charge/discharge analysis at a rate of 83 mA g^{-1} in the potential range between 0.01 V and 3.0 V (*vs.* Li/Li^+). The initial three cycling curves are displayed in Fig. 5a. In the initial cycle, a discharge capacity of approximately 2038 mA h g^{-1} is calculated, which is much higher than the theoretical capacity of MnO_2 (1230 mA h g^{-1}) and the delivered capacities in the following cycles, leading to a low coulombic efficiency of 60%. This extra capacity is assumed from the decomposition of the electrolytes and the further formation of an SEI layer on the anode material surface.[35,47] In the 2nd and 3rd cycles, the curve overlaps and the coulombic efficiency quickly increases to over 90%, suggesting the prominent reversibility and stability of the electrochemical reactions. Meanwhile, the initial three cycles of the CV curves are also measured within the voltage window of 0.01–3 V (*vs.* Li/Li^+) at a scan rate of 0.2 mV s^{-1} to characterize the featured redox reactions and their corresponding potentials during the cycling process (Fig. 5b). In the first cathodic scan, there are several strong and broad peaks below 1.2 V, which are significantly reduced in intensity in the following cycles, partially due to the SEI layer formation.[48] In addition, a clear peak at ~0.4 V in the cathodic scan and two peaks at ~1.2 V and 2.3 V in the anodic scan represent the redox reactions of manganese dioxide, corresponding to the reversible reaction as shown in eqn (8),[20,35] while the peaks at 1.12 V in the cathodic scan and

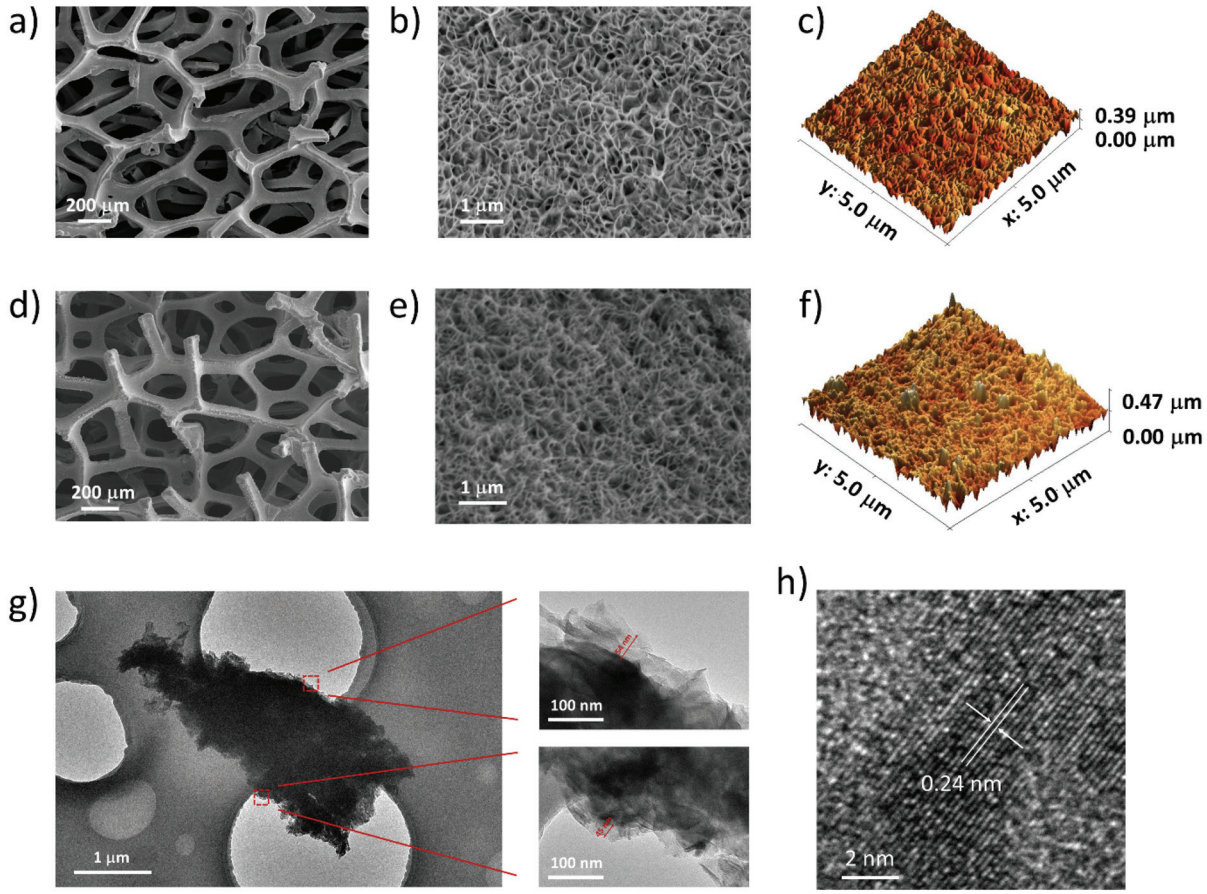

Fig. 4 (a–c) Microstructural characterization of the MnO_2/NF sample: (a) SEM image at low magnification, (b) SEM image at higher magnification and (c) 3D AFM image. (d–f) Microstructural characterization of the MnO_2@PPy/NF-150 sample undergoing 150 s PPy electrodeposition: (d) SEM image at low magnification, (e) SEM image at higher magnification and (f) 3D AFM image. (g) TEM image of MnO_2@PPy/NF. (h) HRTEM image of MnO_2/NF.

1.9 V in the anodic scan matched the conversion between NiO and Ni which has been mentioned above.[34] To estimate the capacity contribution of the NF substrate and the PPy coating, a similar amount of PPy is electrodeposited over the equal-size NF substrate with a mass loading of ~0.1 mg cm^{-2}, in which the CV curve is also measured between 0.01 and 3 V *vs.* Li/Li^+ at a scan rate of 0.2 mV s^{-1} (Fig. 5c). By comparing the occupied area, it is found that the PPy and NF account only for <3% capacity in the composite material of MnO_2@PPy/NF *via* the redox reactions of PPy, which is similar to the reported results in the literature.[47]

$$MnO_2 + 4Li^+ + 4e^- \Leftrightarrow 2Li_2O + Mn \quad (8)$$

$$NiO + 2Li^+ + 2e^- \Leftrightarrow Li_2O + Ni \quad (9)$$

The charge transfer resistance of the electrodes was measured *via* electrochemical impedance spectroscopy (EIS). As shown in Fig. 5d and Fig. S7,† the Nyquist plots of the bare MnO_2/NF, δ-MnO_2@PPy/NF-50 and δ-MnO_2@PPy/NF-150 electrodes show similar trends, but the MnO_2@PPy/NF-150 electrode with a larger amount of PPy coating shows smaller charge transfer resistance due to the superior electrical conductivity of PPy itself, which is beneficial for the faster reaction kinetics. The MnO_2@PPy/NF-150 electrode showed an excellent capacity retention under severe conditions as shown in Fig. 5e. To be specific, the cells undergo galvanostatic charging/discharging for 5 cycles at current rates of 0.08 A g^{-1}, 0.17 A g^{-1}, 0.33 A g^{-1}, 0.67 A g^{-1}, 1.33 A g^{-1}, 2.67 A g^{-1}, 0.08 A g^{-1}, and 0.83 A g^{-1}, in sequence. Notably, high discharge capacities of ~623 mA h g^{-1} and 430 mA h g^{-1} are obtained at high current densities of 1.33 A g^{-1} and 2.67 A g^{-1}, respectively. In addition to the conductive PPy coating on the surface, the highly porous structure formed by the well aligned MnO_2 nanosheets over nickel foam results in a drastically shortened diffusion distance of Li^+ and consequently contributes to the superior rate capability of the composite electrodes. To note, despite the observed decreasing resistance upon the addition of PPy in the EIS results, the rate performances at a current density from 0.08 to 1.3 A g^{-1} do not show many changes. As the EIS test is conducted directly after 12 h of cell assembling, the results may indicate that the electrical conductivity before the galvanostatic test is not the key limiting factor for the rate

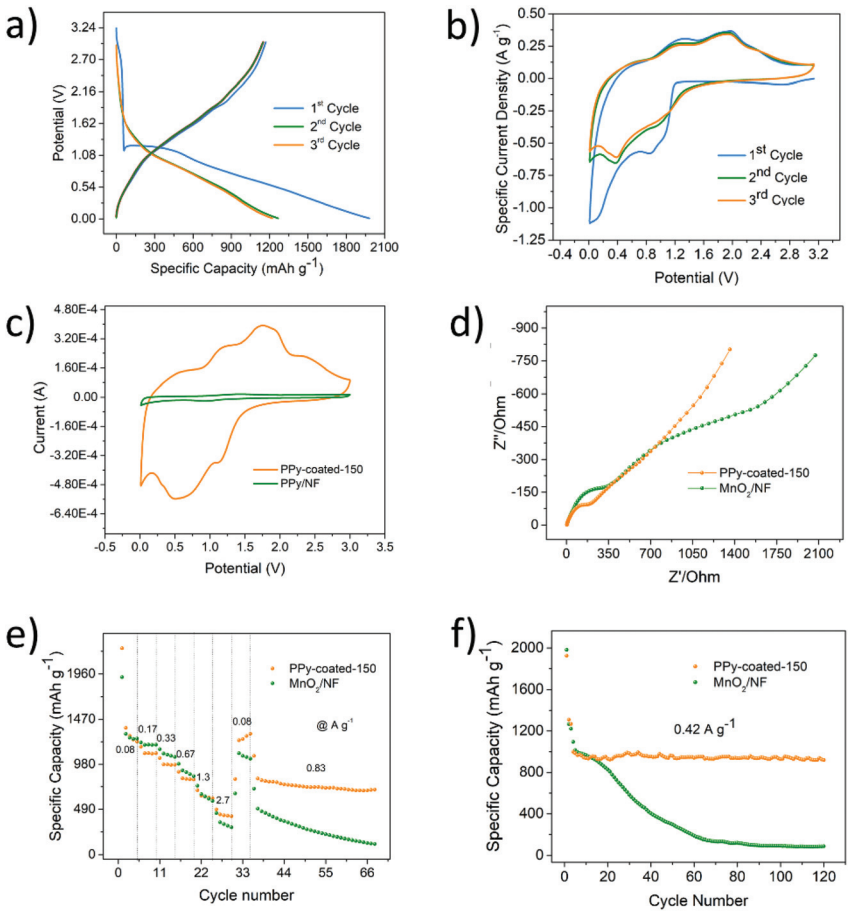

Fig. 5 (a) Galvanostatic charging/discharging curves of the MnO_2@PPy/NF-150 electrode during the first three cycles at a current density of 0.08 A g^{-1}. (b) Cyclic Voltammetry curves of the MnO_2@PPy/NF-150 electrode during the first three cycles at a fixed sweeping rate of 0.2 mV s^{-1}. (c) CV curves of MnO_2@PPy/NF-150 (the black line) and the PPy coated NF (the red line) at the same rate of 0.2 mV s^{-1}. (d) Electrochemical impedance spectra of the bare MnO_2/NF electrodes (black line) and MnO_2@PPy/NF-150 electrodes (the blue line) in the frequency range of 100 kHz–0.01 Hz. (e) Rate capacities of different composite electrodes at various current densities. (f) Cycling performance of the bare MnO_2/NF electrodes (black line) and MnO_2@PPy/NF-150 electrodes (blue line) at a current density of 0.42 A g^{-1}.

capability of the material, while other issues like the SEI formation or material phase transformation process should be considered. In comparison, a much increased capacity is observed with the extension of the cycles upon decreasing the rate to 0.08 A g^{-1} and 0.83 A g^{-1}, suggesting the enhanced reversibility and stability obtained by the PPy coating (Fig. 5e and Fig. S7†). Furthermore, the long-term cycling performances of the bare MnO_2/NF, MnO_2@PPy/NF-150 and MnO_2@PPy/NF-50 electrodes are displayed in Fig. 5f and Fig. S8†, separately. To note, all these electrodes are firstly pre-cycled at 0.08 A g^{-1} for 5 cycles to form a high-qualify SEI layer (stable and even distributed) on their surface. The bare MnO_2/NF electrode shows severe capacity decay, rapidly dropping from 1000 mA h g^{-1} to 20 mA h g^{-1} in the first 80 cycles. In comparison, MnO_2@PPy/NF-50 delivered a better cycling stability, with over 69% capacity retention at the 120th cycle relative to the 6th cycle, while the MnO_2@PPy/NF-150 electrode further improved its cycling stability, with trivial capacity decay in the first few cycles and keeping constant in the following cycles, and delivered an overall capacity retention of over 95% (~930 mA h g^{-1}). This improvement could be ascribed to the improved mechanical and electronic properties of PPy coating and better coverage with the extension of the electrodeposition time, which mechanically suppress the pulverization of the particles and further prevent the loss of active mass during the conversion reaction with large volume expansion.[49,50] Hence, the electrochemical deposition of PPy is supposed to be the optimum approach to achieve the optimum electrochemical performances from the perspectives of charge transfer resistance, rate capability and cyclic stability. Notably, the performances of the composite MnO_2@PPy/NF electrode in our work are comparable and even exceed those of previously reported MnO_2-based anode materials as summarized in Table 1, demonstrating the superiority of our hierarchical structural design in comparison with the merely conductive coating or porous structure counterparts.

The pseudocapacitive behavior of MnO_2@PPy/NF-150 is discussed through analyzing the cyclic voltammetry curves at

Table 1 Electrochemical performances of the designed anode material in this work and the ones reported in previous works

Anode material	Cyclic stability	Rate capability	Ref.
MnO_2 nanorods/rGO	~103% of the initial capacity (~600.3 mA h g^{-1}) at 0.5 A g^{-1} for 650 cycles	811 mA h g^{-1} at 0.1 A g^{-1}, 242.4 mA h g^{-1} at 2 A g^{-1}	51
Mesoporous MnO_2	~94% of the initial capacity (~260 mA h g^{-1}) at 1 A g^{-1} for 200 cycles	905 mA h g^{-1} at 0.1 A g^{-1}, 135 mA h g^{-1} at 2 A g^{-1}	52
MnO_2 nanoparticles	~75% of the initial capacity (~813 mA h g^{-1}) at 0.1 A g^{-1} for 100 cycles	1095 mA h g^{-1} at 0.1 A g^{-1}, 464 mA h g^{-1} at 2 A g^{-1}	53
MnO_2 nanorods/rGO	~70% of the initial capacity (~595 mA h g^{-1}) at 0.1 A g^{-1} for 60 cycles	726 mA h g^{-1} at 0.1 A g^{-1}, 380 mA h g^{-1} at 2 A g^{-1}	54
MnO_2/C hybrid sphere	~99% of the initial capacity (~803 mA h g^{-1}) at 1 A g^{-1} for 60 cycles	1104 mA h g^{-1} at 0.1 A g^{-1}, 354 mA h g^{-1} at 2 A g^{-1}	55
MnO_2@PPy/NF	~95% of the initial capacity (~930 mA h g^{-1}) at 0.42 A g^{-1} for 120 cycles	~1240 mA h g^{-1} at 0.1 A g^{-1}, ~430 mA h g^{-1} at 2.7 A g^{-1}	This work

different scan rates at a voltage window from 0.01 V to 3 V (*vs.* Li/Li^+), as shown in Fig. 6a. The positively shifted peaks in the cathodic scan and negatively moved peaks in the anodic scan with increasing scan rates reveal the larger polarization of the featured electrochemical reactions at higher rates. Furthermore, using the equation $i = av^b$, the capacity contribution from the capacitive effect can be figured out, in which i and v denote the current value and the scan rate, respectively, a is a constant which is small for several parameters and parameter b reflects the originality of the major capacity contribution, with b close to 0.5 indicating an intercalation predominating process while b close to 1 indicating a capacitive predominating one.[56] As the b value for most of the selected points is less than 0.75, the insertion/de-insertion processes other than the capacitive process make the dominant contribution to the overall capacity. Furthermore, by applying the equation, $\frac{i(V)}{v^{\frac{1}{2}}} = K_1 v^{1/2} + k_2$, in which the former term represents the current contribution from ion intercalation and the later one corresponds to the current contribution from the surface capacitive effect, the capacitive contribution ratio under different scan rates is figured out and summarized in Fig. 6b and c. To be specific, the pseudocapacitive contributions at a rate of 0.2, 0.3, 0.5, 0.8, 1.2, and 1.5 mV s^{-1} are 24%, 27%, 32%, 38%, 43%, and 49%, respectively. This suggests the increasing importance of the pseudocapacitive effect on the electrochemical performances at higher sweeping rates as a result of the limitation of Li^+ diffusion capability in the electro-

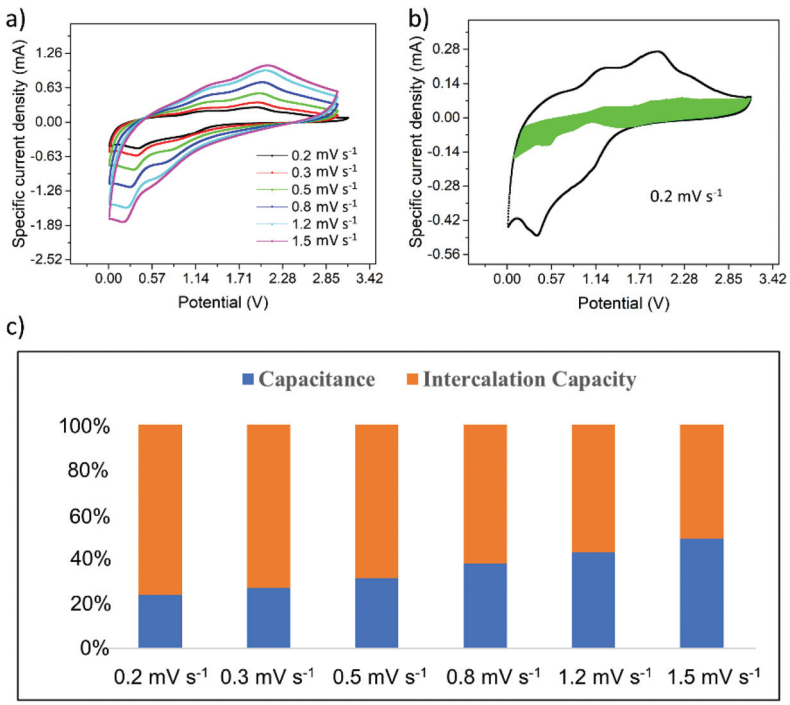

Fig. 6 Comparison of (a) the CV curves at different current rates. (b) CV curve of the composite MnO_2@PPy/NF-150 electrode with separation between the overall current (black line) and pseudocapacitive current (light green area). (c) Comparison of the pseudocapacitive contribution to the overall capacity at different sweeping rates.

lytes, which to some extent contributes to the superior rate capability of the composite material at higher rates.[56]

4 Conclusions

A highly porous MnO_2@PPy/NF-150 anode was synthesized by the hydrothermal growth of MnO_2 nanosheets over NF followed by the electrodeposition of PPy on the surface. As anodes for LIBs, the composite material delivered good cycling performance with ~970 mA h g^{-1} capacity at 0.42 A g^{-1}, retaining 95% capacity after over 120 cycles, and good rate capability with ~430 mA h g^{-1} discharging capacity at a high current density of 2.67 A g^{-1}, which are competitive and even surpassing those of reported MnO_2-based anode materials. To note, the synergistic effects of the conductive PPy coating, nanosheet morphology and 3D conductive hosts help buffer the severe volume variation of MnO_2 during the conversion reaction and achieve such a good cycling stability, suggesting a promising route for designing anode materials for LIBs

Conflicts of interest

There are no conflicts to declare.

Acknowledgements

This work was supported by the National Science Foundation (CBET 1803256), the Local Innovative and Research Teams Project of Guangdong Pearl River Talents Program (2017BT01N111) and the Shenzhen Government (Project No. JCYJ20170412171720306 & JSGG20170414143635496).

References

1 S. Vazquez, *et al.*, Energy Storage Systems for Transport and Grid Applications, *IEEE Trans. Ind. Electron.*, 2010, **57**(12), 3881–3895.
2 Y. Sui, *et al.*, Dual-ion batteries: The emerging alternative rechargeable batteries, *Energy Storage Mater.*, 2020, **25**, 1–32.
3 N. Nitta, *et al.*, Li-ion battery materials: present and future, *Mater. Today*, 2015, **18**(5), 252–264.
4 D. P. DiVincenzo and E. J. Mele, Cohesion and structure in stage-1 graphite intercalation compounds, *Phys. Rev. B: Condens. Matter Mater. Phys.*, 1985, **32**(4), 2538–2553.
5 J. Jiang and J. R. Dahn, Effects of solvents and salts on the thermal stability of LiC6, *Electrochim. Acta*, 2004, **49**(26), 4599–4604.
6 S. H. Yu, *et al.*, Conversion Reaction-Based Oxide Nanomaterials for Lithium Ion Battery Anodes, *Small*, 2016, **12**(16), 2146–2172.
7 M.-S. Wang, *et al.*, Scalable preparation of porous micron-SnO2/C composites as high performance anode material for lithium ion battery, *J. Power Sources*, 2016, **309**, 238–244.
8 H. Liu, *et al.*, Rational design of TiO2@ nitrogen-doped carbon coaxial nanotubes as anode for advanced lithium ion batteries, *Appl. Surf. Sci.*, 2018, **458**, 1018–1025.
9 C. Zhu, *et al.*, TiO2 nanotube @ SnO2 nanoflake core–branch arrays for lithium-ion battery anode, *Nano Energy*, 2014, **4**, 105–112.
10 N. Mahmood, T. Tang and Y. Hou, Nanostructured Anode Materials for Lithium Ion Batteries: Progress, Challenge and Perspective, *Adv. Energy Mater.*, 2016, **6**(17), 1600374.
11 M. V. Reddy, G. V. Subba Rao and B. V. R. Chowdari, Metal oxides and oxysalts as anode materials for Li ion batteries, *Chem. Rev.*, 2013, **113**(7), 5364–5457.
12 L. Li, A.-R. O. Raji and J. M. Tour, Graphene-Wrapped MnO2–Graphene Nanoribbons as Anode Materials for High-Performance Lithium Ion Batteries, *Adv. Mater.*, 2013, **25**(43), 6298–6302.
13 J. Zang, *et al.*, Hollow carbon sphere with open pore encapsulated MnO2 nanosheets as high-performance anode materials for lithium ion batteries, *Electrochim. Acta*, 2018, **260**, 783–788.
14 N. Yu, *et al.*, *In situ* growth of binder-free hierarchical carbon coated CoSe2 as a high performance lithium ion battery anode, *Appl. Surf. Sci.*, 2019, **483**, 85–90.
15 B. Jia, *et al.*, Construction of MnO2 Artificial Leaf with Atomic Thickness as Highly Stable Battery Anodes, *Adv. Mater.*, 2020, **32**(1), 1906582.
16 C. X. Guo, *et al.*, A Hierarchically Nanostructured Composite of MnO2/Conjugated Polymer/Graphene for High-Performance Lithium Ion Batteries, *Adv. Energy Mater.*, 2011, **1**(5), 736–741.
17 J. Qin, *et al.*, MnOx/SWCNT macro-films as flexible binder-free anodes for high-performance Li-ion batteries, *Nano Energy*, 2013, **2**(5), 733–741.
18 S. Fu, *et al.*, Hydrogenation Driven Conductive Na2Ti3O7 Nanoarrays as Robust Binder-Free Anodes for Sodium-Ion Batteries, *Nano Lett.*, 2016, **16**(7), 4544–4551.
19 Y. Li, *et al.*, Free-standing reduced graphene oxide/MnO2–reduced graphene oxide–carbon nanotube nanocomposite flexible membrane as an anode for improving lithium-ion batteries, *Phys. Chem. Chem. Phys.*, 2017, **19**(11), 7498–7505.
20 X. Zhou, *et al.*, Embedding MnO2 Ultrafine Nanoparticles within Graphene-Based Hybrid Elastomer as an Anode for Enhanced Lithium Storage, *ChemElectroChem*, 2018, **5**(16), 2310–2315.
21 T. Gao, *et al.*, Biomass-Derived Carbon Paper to Sandwich Magnetite Anode for Long-Life Li-Ion Battery, *ACS Nano*, 2019, **13**(10), 11901–11911.
22 W. Bi, *et al.*, V2O5–Conductive polymer nanocables with built-in local electric field derived from interfacial oxygen vacancies for high energy density supercapacitors, *J. Mater. Chem. A*, 2019, **7**(30), 17966–17973.
23 Y.-S. Chen, *et al.*, Gas sensitivity of a composite of multi-walled carbon nanotubes and polypyrrole prepared by vapor phase polymerization, *Carbon*, 2007, **45**(2), 357–363.

24 Y. S. Lim, *et al.*, Polypyrrole/graphene composite films synthesized via potentiostatic deposition, *J. Appl. Polym. Sci.*, 2013, **128**(1), 224–229.
25 L. Han, P. Tang and L. Zhang, Hierarchical Co3O4@PPy@MnO2 core–shell–shell nanowire arrays for enhanced electrochemical energy storage, *Nano Energy*, 2014, **7**, 42–51.
26 Z. Ren, *et al.*, Large-scale synthesis of hybrid metal oxides through metal redox mechanism for high-performance pseudocapacitors, *Sci. Rep.*, 2016, **6**(1), 20021.
27 R. H. Petrucci, W. S. Harwood and F. G. Herring, *General Chemistry Principles and Modern Applications*, Prentice Hall, Englewood Cliffs, 2002.
28 D. R. Lide, *Handbook of Chemistry and Physics*, CRC Press LLC, Boca Raton, 2004.
29 R. W. Bosch, D. Féron and J. P. Celis, *Electrochemistry in Light Water Reactors*, CRC Press, 2007.
30 F. Conzuelo, *et al.*, The Open Circuit Voltage in Biofuel Cells: Nernstian Shift in Pseudocapacitive Electrodes, *Angew. Chem., Int. Ed.*, 2018, **57**(41), 13681–13685.
31 S. Saha, *et al.*, *In situ* hydrothermal synthesis of MnO2/NiO@Ni hetero structure electrode for hydrogen evolution reaction and high energy asymmetric supercapacitor applications, *J. Energy Storage*, 2016, **6**, 22–31.
32 Y. Zhao, *et al.*, Defect-Engineered Ultrathin δ-MnO2 Nanosheet Arrays as Bifunctional Electrodes for Efficient Overall Water Splitting, *Adv. Energy Mater.*, 2017, **7**(18), 1700005.
33 X.-B. Cheng, *et al.*, Toward Safe Lithium Metal Anode in Rechargeable Batteries: A Review, *Chem. Rev.*, 2017, **117**(15), 10403–10473.
34 B. Varghese, *et al.*, Fabrication of NiO Nanowall Electrodes for High Performance Lithium Ion Battery, *Chem. Mater.*, 2008, **20**(10), 3360–3367.
35 H. Liu, *et al.*, Reduced graphene oxide anchored with δ-MnO2 nanoscrolls as anode materials for enhanced Li-ion storage, *Ceram. Int.*, 2016, **42**(12), 13519–13524.
36 H. Chen, *et al.*, One-Step Fabrication of Ultrathin Porous Nickel Hydroxide-Manganese Dioxide Hybrid Nanosheets for Supercapacitor Electrodes with Excellent Capacitive Performance, *Adv. Energy Mater.*, 2013, **3**(12), 1636–1646.
37 D. Yan, *et al.*, Fabrication, In-Depth Characterization, and Formation Mechanism of Crystalline Porous Birnessite MnO2 Film with Amorphous Bottom Layers by Hydrothermal Method, *Cryst. Growth Des.*, 2009, **9**(1), 218–222.
38 X. Xie, *et al.*, Controlled Fabrication of High-Quality Carbon Nanoscrolls from Monolayer Graphene, *Nano Lett.*, 2009, **9**(7), 2565–2570.
39 E. Garfias-García, *et al.*, Mechanism and kinetics of the electrochemical formation of polypyrrole under forced convection conditions, *J. Electroanal. Chem.*, 2008, **613**(1), 67–79.
40 S. B. Saidman and J. B. Bessone, Electrochemical preparation and characterisation of polypyrrole on aluminium in aqueous solution, *J. Electroanal. Chem.*, 2002, **521**(1), 87–94.
41 M. Grzeszczuk, J. Kalenik and A. Kępas-Suwara, Phase boundaries in layer-by-layer electrodeposited polypyrrole resulted from 2D–3D growths of polymer sublayers, *J. Electroanal. Chem.*, 2009, **626**(1), 47–58.
42 M. Mylarappa, *et al.*, A facile hydrothermal recovery of nano sealed MnO2particle from waste batteries: An advanced material for electrochemical and environmental applications, *IOP Conf. Ser.: Mater. Sci. Eng.*, 2016, **149**, 012178.
43 I. Sultana, *et al.*, Electrodeposited polypyrrole (PPy)/para (toluene sulfonic acid) (pTS) free-standing film for lithium secondary battery application, *Electrochim. Acta*, 2012, **60**, 201–205.
44 J. Li, L. Cui and X. Zhang, Preparation and electrochemistry of one-dimensional nanostructured MnO2/PPy composite for electrochemical capacitor, *Appl. Surf. Sci.*, 2010, **256**(13), 4339–4343.
45 K. Liang, *et al.*, In situ synthesis of SWNTs@MnO2/polypyrrole hybrid film as binder-free supercapacitor electrode, *Nano Energy*, 2014, **9**, 245–251.
46 U. O. Aigbe, *et al.*, Removal of hexavalent chromium from wastewater using PPy/Fe3O4 magnetic nanocomposite influenced by rotating magnetic field from two pole three-phase induction motor, *J. Phys.: Conf. Ser.*, 2018, **984**, 012008.
47 S. A. Hashmi, A. Kumar and S. K. Tripathi, Investigations on electrochemical supercapacitors using polypyrrole redox electrodes and PMMA based gel electrolytes, *Eur. Polym. J.*, 2005, **41**(6), 1373–1379.
48 W. Gou, *et al.*, Yolk-shell structured V2O3 microspheres wrapped in N, S co-doped carbon as pea-pod nanofibers for high-capacity lithium ion batteries, *Chem. Eng. J.*, 2019, **374**, 545–553.
49 J. Liu, *et al.*, Three dimensionals α-Fe2O3/polypyrrole (Ppy) nanoarray as anode for micro lithium ion batteries, *Nano Energy*, 2013, **2**(5), 726–732.
50 J. Liu, *et al.*, Uniform Hierarchical Fe3O4@Polypyrrole Nanocages for Superior Lithium Ion Battery Anodes, *Adv. Energy Mater.*, 2016, **6**(13), 1600256.
51 Z. Ma and T. Zhao, Reduced graphene oxide anchored with MnO2 nanorods as anode for high rate and long cycle Lithium ion batteries, *Electrochim. Acta*, 2016, **201**, 165–171.
52 A. A. Voskanyan, C.-K. Ho and K. Y. Chan, 3D δ-MnO2 nanostructure with ultralarge mesopores as high-performance lithium-ion battery anode fabricated via colloidal solution combustion synthesis, *J. Power Sources*, 2019, **421**, 162–168.
53 L. Zhang, *et al.*, Tailoring nanostructured MnO2 as anodes for lithium ion batteries with high reversible capacity and initial Coulombic efficiency, *J. Power Sources*, 2018, **379**, 68–73.
54 H. Liu, *et al.*, MnO2 nanorods/3D-rGO composite as high performance anode materials for Li-ion batteries, *Appl. Surf. Sci.*, 2017, **392**, 777–784.

55 G. Wang, *et al.*, Constructing Hierarchically Hollow Core–Shell MnO2/C Hybrid Spheres for High-Performance Lithium Storage, *Small*, 2016, **12**(29), 3914–3919.

56 J. Wang, J. P. James Lim and B. Dunn, Pseudocapacitive Contributions to Electrochemical Energy Storage in TiO2 (Anatase) Nanoparticles, *J. Phys. Chem. C*, 2007, **111**(40), 14925–14931.